remote sensing

MDPI

Article

Structural Assessment via Ground Penetrating Radar at the Consoli Palace of Gubbio (Italy)

Ilaria Catapano [1,*], Giovanni Ludeno [1], Francesco Soldovieri [1], Francesco Tosti [2] and Giuseppina Padeletti [3]

1 Institute for Electromagnetic Sensing of the Environment, National Research Council of Italy, I-80124 Napoli, Italy; ludeno.g@irea.cnr.it (G.L.); soldovieri.f@irea.cnr.it (F.S.)
2 Municipality of Gubbio, Piazza Grande, 9, I-06024 Gubbio (PG), Italy; f.tosti@comune.gubbio.pg.it
3 Institute for the Study of Nanostructured Materials, National Research Council of Italy, P.le Aldo Moro, 5, I-00185 Rome, Italy; giuseppina.padeletti@ismn.cnr.it
* Correspondence: catapano.i@irea.cnr.it

Received: 15 November 2017; Accepted: 21 December 2017; Published: 28 December 2017

Abstract: Ground Penetrating Radar (GPR) is a flexible and cost-effective tool for performing structural integrity assessment and quick damage evaluation of manmade structures, including cultural heritage (CH) assets. In this context, this paper deals with the usefulness of GPR surveys enhanced by the use of a Microwave Tomographic data processing approach as a methodology for the diagnosis and monitoring of CH exposed to climate events and natural hazards. Specifically, the paper reports on the results of a measurement campaign carried out at the Loggia of the Consoli Palace of Gubbio (Italy). These results allowed us to increase our knowledge of the architecture of the surveyed zones and their structural hazards.

Keywords: radar imaging; microwave tomography; structural surveys; cultural heritage

1. Introduction

European Cultural Heritage (CH) assets such as monuments, historical centers and archaeological landscapes are affected by a process of decline, which is occurring at an alarming rate due to natural aging, human impact, environmental and climatic changes, and natural hazards [1]. Accordingly, a great deal of attention is directed towards the implementation of diagnosis and monitoring technologies and their joint use. Indeed, the collection and integration of data provided by different novel and state-of-the-art technologies operating at different spatial scales (from wide areas to single structures and their elements) and on different observation platforms (e.g., satellite, airborne, and on-site) allow, in principle, a multi-temporal and multi-spatial situational awareness.

In this context, Ground Penetrating Radar (GPR), an in situ electromagnetic sensing technique, is attracting interest since it allows non-destructive and non-invasive subsurface analysis, providing useful information for structural assessment and characterization of environmental hazards such as hydrological risks. GPR surveys, indeed, can be carried out at different carrier frequencies, depending on the antenna system adopted; thus, different measurement resolutions and penetration depths can be reached.

Nowadays, GPR is a well-assessed technology that is widely employed in several applicative contexts [2]. Regarding CH assets, GPR is useful for investigating deformation of hollow piers due to mechanical stress [3], and for studying the signal reflected by objects inside structures such as bridges or viaducts [4–7]. Moreover, it allows us to analyze the state of conservation of ancient buildings from historical, archaeological, and structural points of view [8–12]. These examples represent only a small portion of the wide existing literature.

However, despite this widespread use, GPR effectiveness depends significantly on the users' ability to interpret the obtained images, i.e., the radargrams. Indeed, a radargram provides a distorted image of the scenario under test, which can lead to incorrect readings of the information gathered. As a consequence, there is a continuing interest in the development and use of application-oriented data-processing approaches capable of providing easily interpretable images [2–4,6,13–19].

Among these, microwave tomographic approaches, which address imaging as the solution of an inverse scattering problem [20], are worth considering, and continuous efforts are being focused on the employment of microwave tomography enhanced GPR and its application-oriented optimization.

This paper deals with this issue, and aims to present the imaging results obtained by using a commercial time-domain GPR system and a two-step data-processing strategy. The first step of the data processing employs widely used filtering procedures, which are chosen by taking into account the peculiarities of the investigated scenario, i.e., the kinds of targets that are expected to be reconstructed. The second step involves a microwave tomographic approach, which is based on a linear model of the scattering phenomenon underlying the GPR survey, and has previously been employed successfully in several applicative contexts [13–16,21]. In this context, it is worth noting that none of the procedures employed in the data processing strategy are new, but the advantages in terms of imaging capabilities offered by their combined use remains an open issue.

The results provided concern a measurement campaign carried out at the Consoli Palace of Gubbio in July 2017; specifically, they regard the Loggia, which is a part of the Consoli Palace requiring monitoring, since it is affected by several crack patterns. The results presented herein make a valuable contribution in terms of improving the available knowledge of the significant crack pattern affecting the cross-hall leading to the Loggia, and provides clues regarding the structure of the Loggia walls.

2. Instrumentation and Imaging

2.1. Measurement Device

The raw data have been gathered by using the IDS manufactured RIS K2_FW GPR system [22] equipped with a 2 GHz single-fold shielded antenna, which is shown in Figure 1. The RIS K2_FW is a time-domain system, whose architecture is made up of three main components:

Figure 1. RIS K2_FW GPR system.

- the electronic unit, which drives and commands the transmission and reception of the signal, and digitalizes the measured signal;
- the antenna system, which transmits the field impinging on the target, and receives the field backscattered by the target;

- the processing/monitor unit, i.e., the laptop, which controls the data acquisition and performs data elaboration and visualization, as well as storage of the collected waveforms. These tasks are performed by means of dedicated software.

The three main components are connected to each other by wiring cables; specifically, the control unit is connected to the processing unit by a LAN (Local Area Network) cable, and to the antenna system by means of a 19-pin connector. Moreover, the control unit is powered by an external battery, while the laptop has its own power bank.

Before starting the measurement procedure, the operator must configure the system by selecting the antenna type (among the models provided into the system library), the observation time window and the number of samples, discretizing the waveform acquired at each measurement point.

For the measurement procedure considered herein, the TRHF model, which corresponds to the adopted antenna, a 32 ns time window, and 512 samples were adopted. Each radargram, or B-Scan, was gathered by moving the system by hand along the measurement line, i.e., a straight trace. A survey wheel synchronized spatial movement and data acquisition. The gathered waveforms were saved in ASCII format and processed off line.

2.2. Data Processing

A two-step data processing strategy, whose use is made feasible for non-expert users thanks to a graphical interface [23], was adopted. The two main steps of the strategy are pre-processing and the data inversion.

2.2.1. Pre-Processing

The pre-processing consists of standard time-domain (TD) procedures, commonly performed by GPR users to remove direct antenna coupling, to reduce noise, and to improve the target footprint.

Specifically, TD data processing begins with start time correction and involves procedures such as time gating (TG) and back-ground (BG) removal, which help to remove or mitigate the signal contributions due to antenna coupling, air-material interface and (undesired) horizontal reflectors [2]. Figure 2 shows an example of a raw radargram and its filtered version by means of the above-cited TD filtering procedures; such a figure is representative of the data taken as input for the microwave tomographic approach. Indeed, by taking into account the specific features of the investigated site (see Section 3) and, specifically, the fact that a satisfactory characterization requires the simultaneous imaging of both surface and deep objects, which could be either extended or point-like targets, both TG and BG removal are used, after which the time zero correction is performed (see Figure 2b,c).

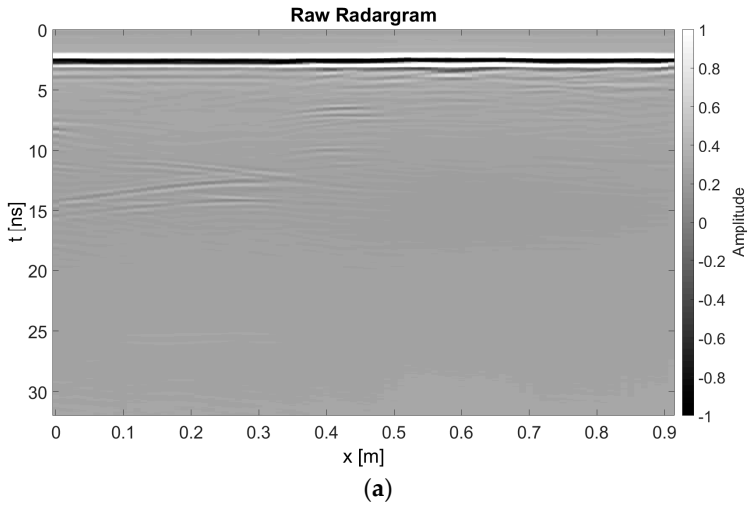

(**a**)

Figure 2. *Cont.*

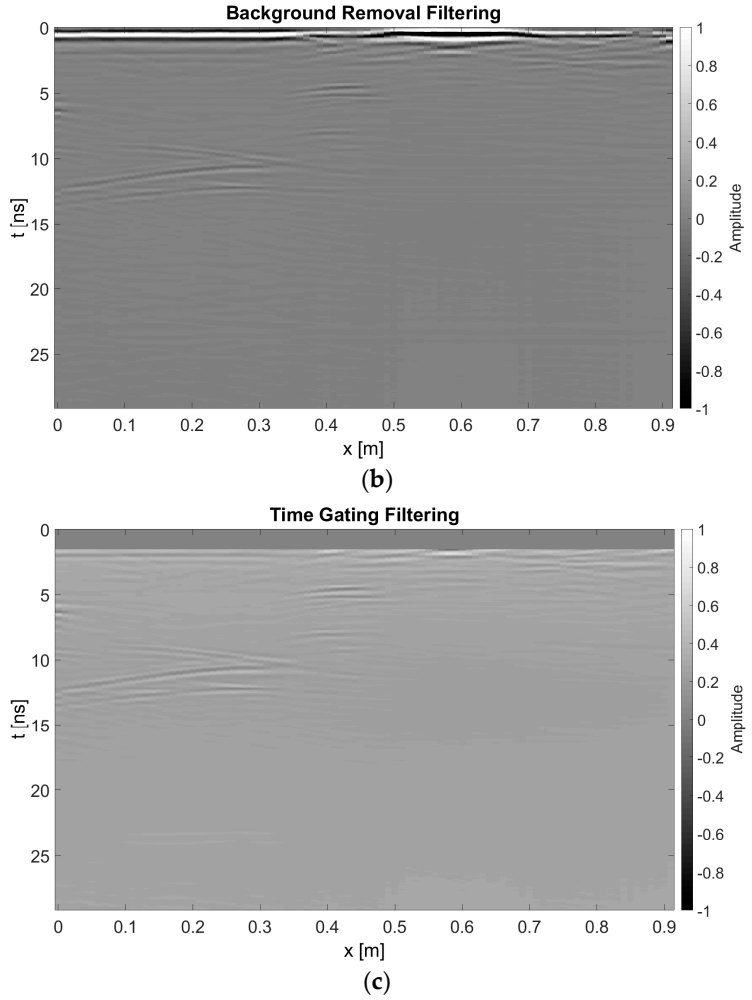

Figure 2. (**a**) Raw radargram; (**b**) radargram after time zero correction and background removal filtering; (**c**) radargram after time zero correction and time gating filtering.

In particular, let us note that the BG removal procedure allows us to remove the antenna direct coupling while providing information on the surface targets, but it removes or modifies information about buried interfaces or extended objects. Conversely, TG allows the preservations of such information but, together with the direct antenna coupling and the signal contribution due to the air-medium interface, it also removes data accounting for surface targets. Accordingly, in the adopted pre-processing step, BG removal is exploited to reconstruct the shallow portion of the investigated scenario, while TG procedure is employed to obtain an accurate characterization of the deep part.

2.2.2. Data Inversion

The data inversion addresses the imaging as the solution of an inverse scattering problem and utilizes the Born approximation to define the mathematical model describing the relationship between data and unknowns [2,13,14]. Specifically, the applied approach processes a single GPR profile (radargram) under the assumption of a 2D scalar geometry. Therefore, the surveyed medium is supposed to be a homogeneous space, having relative dielectric permittivity ε_b. The targets are cylinders with arbitrary cross section and are looked for as electromagnetic anomalies having a relative dielectric permittivity ε_x. Accordingly, the imaging approach considers as unknown the contrast function $\chi(r) = \varepsilon_x(r)/\varepsilon_b - 1$, which represents the relative difference between the permittivity of the targets and the permittivity of the surveyed medium.

According to the features of the GPR system, a multi-monostatic and multi-frequency measurement configuration is assumed and the transmitting antenna is modeled as a filamentary line source directed along the invariance axis.

According to these assumptions, the scattering phenomenon is described, at each angular frequency ω, by the integral equation [2,20]:

$$E_s(x_s, x_0, \omega) = k_b^2 \int_{\Omega} G(x_0, \omega, r) E_{inc}(x_s, \omega, r) \chi(r) dr \quad (1)$$

where E_s denotes the scattered field measured in x_0 when the probing source is in $x_s = x_0$, E_{inc} is the incident field in Ω, i.e., the field in the probed region in the absence of any target, k_b is the wave number in the background medium, and G is the known Green's function referring to the scenario at hand [2]. The integral Equation (1) is discretized in order to achieve the matrix equation:

$$\mathbf{E}_s = \mathbf{L}[\chi] \quad (2)$$

where $\mathbf{E}_s$ is the (M × F)-dimensional data vector, M and F being the number of work measurement points and frequencies, respectively; $\mathbf{L}$ is the (M × F) × N dimensional matrix, N being the number of pixels into the investigated domain Ω. Therefore, the matrix $\mathbf{L}$ relates the N-dimensional unknown vector χ (contrast function) to the data vector $\mathbf{E}_s$ (scattered field).

The linear system in (2) is ill-conditioned and its stable approximate solution can be easily obtained by computing the Singular Value Decomposition (SVD) of the matrix $\mathbf{L}$ [24]. By exploiting the Truncated SVD (TSVD) as a regularization scheme, an approximated expression of the unknown contrast values in Ω is given by:

$$\hat{\chi} = \sum_{n=1}^{T} \frac{1}{\sigma_n} \langle \mathbf{E}_s, \mathbf{u}_n \rangle \mathbf{v}_n \quad (3)$$

In (3), σ_n is the n-th singular value of the matrix $\mathbf{L}$, while $\mathbf{v}_n$ and $\mathbf{u}_n$ are its n-th left and right singular vectors, $<\cdot,\cdot>$ denotes the scalar product in the data space. The threshold $T \leq \min\{(M \times F), N\}$ is set in such a way to assure a good trade-off between accuracy and stability of the results and according to the level of noise on data [2,13].

The output of the processing chain is a spatial map, referred to as a tomographic image, showing, pixel by pixel, the absolute value of the retrieved contrast function, whose expression is given by Equation (3), as normalized to its maximum value (into the investigated region). Accordingly, the significant values identify the location of targets and give information about target geometry.

Before concluding this sub-Section, it is worth noting that the relative permittivity of the investigated medium, ε_b, is an important parameter of the imaging procedure. It is worth noting that one needs an accurate knowledge of ε_b, i.e., of the electromagnetic wave propagation velocity, v, (which is given by $v = c/\sqrt{\varepsilon_b}$, with c being the wave velocity in free space), in order to provide an accurate localization of the targets. Specifically, in the frame of linear microwave tomography, an inaccurate knowledge of ε_b or v determines an under/over-estimation of the target position [25]. Accordingly, part of the GPR literature is focused on methods for estimating v, and strategies based on hyperbola-fitting or the use of Time Domain Reflectometry (TDR) measurements have been proposed [26,27]. As detailed in Section 3.2, herein, ε_b, and thus v, is estimated from one of the processed datasets by taking into account that it is referred to a portion of wall whose thickness is known, i.e., it is measurable in situ.

3. Test Site and Results

3.1. The Consoli Palace

The Consoli Palace is the symbol of Gubbio (Italy) and is the most representative and spectacular building of the whole monumental town. It was built between 1332 and 1349, together with a daring pensile square ("Piazza Grande") in the heart of the four districts of the city, see Figure 3a.

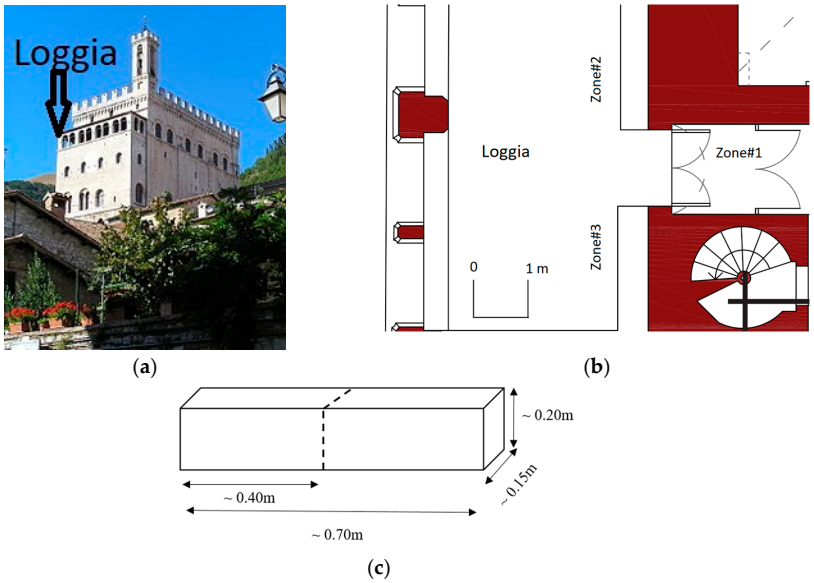

Figure 3. (**a**) Consoli Palace; (**b**) layout of the investigated areas; (**c**) typical stone block used for the construction of the exterior walls of the Consoli Palace.

The Palace is made mainly from limestone, travertine, sandstones, plasters, blinders and mortars. Moreover, it has a rectangular shape, and a very articulated distribution of volumes. It was, indeed, erected on the slope of the mountain and has its foundations placed on two different levels, due to the local topography. This aspect confers to the west side of the structure a remarkable height of about 60 m. The difference in height of the two levels of the foundations is about 10 m. Such a difference, together with environmental actions and other natural hazards (e.g., earthquakes) could be the reasons for differential displacements.

At present, the effects of these differential displacements are visible in the west wall and in the cross hall of the Loggia in the form of activated local mechanisms and crack patterns. The main critical aspect is highlighted in the south-west part, where an out-of-plane rocking mechanism is becoming evident by a widespread crack pattern. For this reason, the Consoli Palace was used as one of the test sites of the HERACLES project, and several sensing technologies, among them GPR, are currently employed to investigate its structural assets.

In this context, a GPR measurement procedure was performed on 12 July 2017 at the Loggia of the Consoli Palace; specifically at the areas denoted as Zone#1, Zone#2 and Zone#3 in Figure 3b, which shows the layout of the portion of the Loggia mainly affected by visible crack patterns. The surveys were performed by using the GPR system described in Section 2.1.

Figure 3c depicts a sketch of a typical stone block used for building the perimeter walls of the Consoli Palace, whose dimensions are: Length 0.40 m/0.70 m, Width 0.15 m and Height 0.20 m.

3.2. GPR Survey Results

This Subsection Describes the Results Provided by the Elaboration of the Raw GPR Data by Means of the Approach Described in Section 2.2.

It is worth pointing out that the data inversion has been performed by assuming that the surveyed media are characterized by a relative permittivity, whose average value was fixed at 4. This value was estimated by the data collected at Zone#1 by taking into account the information on wall thickness, and is consistent with the relative permittivity of sandstone [28]. Moreover, the effective frequency range of the data has been estimated by means of spectral analysis. This from 800 MHz to 2050 MHz, and was sampled at 51 evenly spaced frequencies. Finally, the TSVD threshold was such that it filtered out all of the singular values whose value was 25 dB lower than the maximum one.

3.2.1. Zone#1

At the cross-hall leading to the Loggia, GPR data were collected on a surface of about 1 m^2, whose side was 0.96 m along the *x*-axis and 1.2 m along *y*-axis, according to the coordinate reference system depicted in Figure 4. As Figure 4 shows, cardboard was applied on the investigated region during the measurement step. Data were gathered with a 0.01 m spatial offset by moving the antenna from left to right along the *x*-axis, and by considering 25 traces, spaced 0.05 m apart, along the *y*-axis.

Figure 4. Measurement setup at Zone#1.

Figure 5a–f shows a picture of the surveyed Zone without the cardboard, and the tomographic images at constant and increasing depths. Specifically, Figure 5b–d shows the tomographic images at depths z = 0.03 m, z = 0.07 m and z = 0.12 m, respectively, which have been obtained using BG removal in the pre-processing step. Conversely, Figure 5e,f, which shows the tomographic images at z = 0.50 m and z = 0.70 m, respectively, were obtained using the TG procedure.

The crack pattern, three main cavities, and the arrangement of the stone blocks are clearly recognizable by means of a visual inspection, see Figure 5a. In particular, one can observe that:

- the crack occurred at the junction area between two different types of walls, a stone wall (left) and a brick wall (right)—the junction area is marked by two vertical red lines;
- the cavities are due to the fall of some bricks, maybe due to wall fracture;
- the stone wall is made up of alternating stone blocks with lengths of 0.40 m and 0.70 m, see Figure 5a.

Moreover, based on Figure 3b, it is worth noting that the thickness of the brick walls is about 0.70 m, and that the bricks are not as high as the stone blocks.

The analysis of the GPR data acquired in Zone#1 not only confirms the information provided by the visual inspection, but also increases the amount of information available about the crack and the wall textures. Indeed, the crack pattern, the three main cavities, and the alternating stone blocks with different length are clearly visible in Figure 5b. Moreover, based on Figure 5c, wherein the 3rd cavity is

not clearly visible, one can infer that this cavity is less deep than the other two cavities and the crack pattern, while according to Figure 5d, wherein only the first cavity is still present, one would expect that the crack reaches a depth no greater than about 0.10 m.

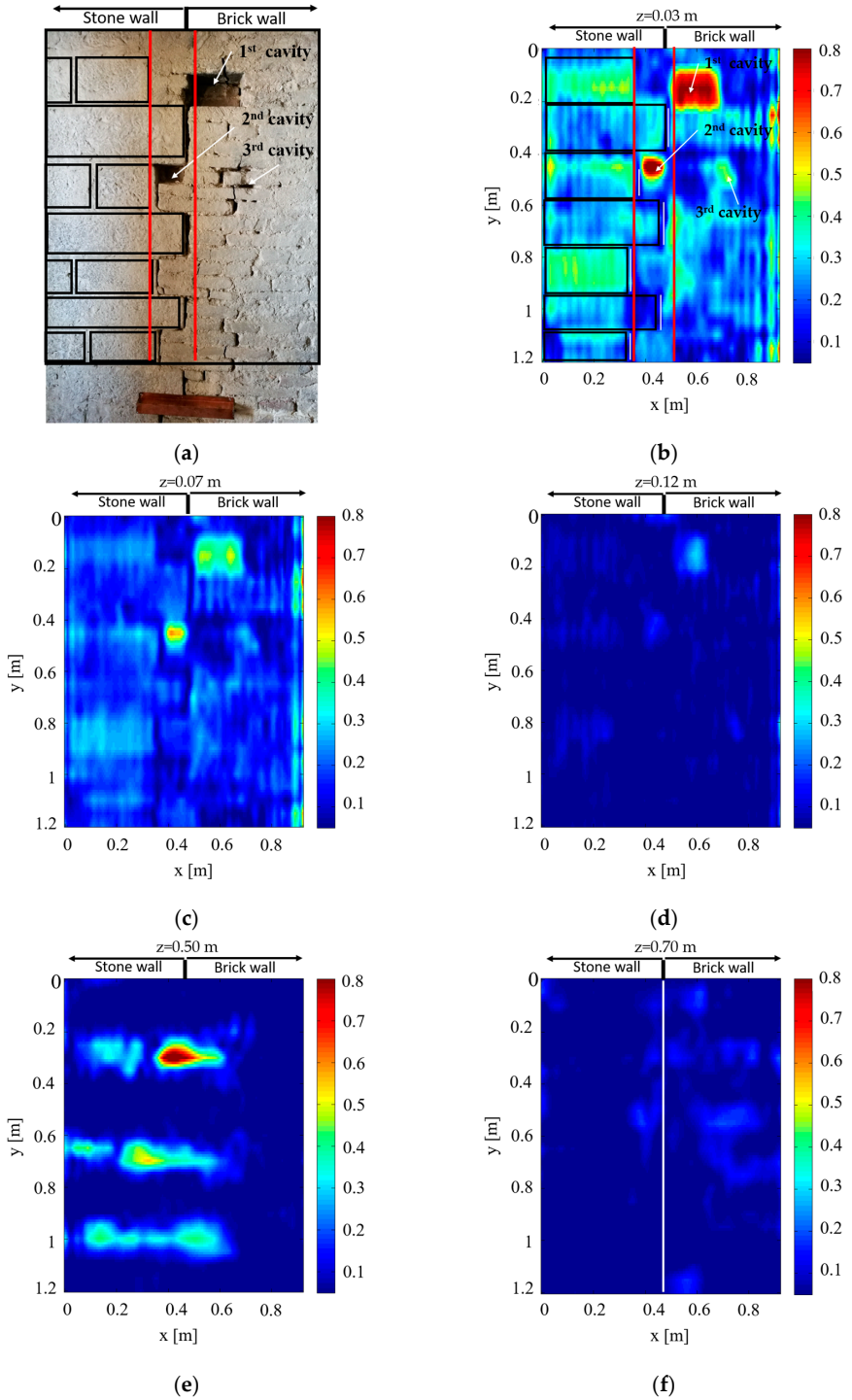

Figure 5. The crack pattern and the three main cavities in Zone#1: (**a**) picture of the crack pattern and the three main cavities on the wall along the Loggia cross hall. The red lines delimit the junction area; (**b**–**f**) tomographic image at z = 0.03 m, z = 0.07 m, z = 0.12 m., z = 0.50 m, z = 0.70 m. The tomographic images show the normalized intensity of the obtained contrast.

In addition, Figure 5e shows three long stone blocks, which were potentially employed for the junction of the walls, while Figure 5f shows the interface between stone and brick walls, which is marked by the vertical white line. In Figure 5f, the texture of the brick wall is recognizable due to the occurrence, at this depth, of the backside of the wall, i.e., the brick wall-air interface. The thickness of the brick wall is indeed about 75 cm.

The sequence of the tomographic images at increasing constant depths obtained by exploiting both the BG removal and TG procedures are shown in the Supplementary materials, in Figure S1. In this file, the depth slices from z = 0.01 m and z = 0.20 m were obtained by using BG removal, while the other one was obtained using the TG procedure. The results in Figure 5b–e have been extracted by the content of the multimedia file Figure S1.

3.2.2. Zone#2 and Zone#3

The other two investigated regions, i.e., Zone#2 and Zona#3, are located on the west wall of the Loggia (see Figure 3b). This wall is part of the outside perimeter of the Consoli Palace, and it is made up of parallelepiped stone blocks, see Figure 6a,b, that depict the two regions, respectively.

At Zone#2, GPR data were acquired on an area of about 1 m^2, while at Zone#3 the surveyed area was about 0.85 m^2. Specifically, according to the coordinate reference system in Figure 6, the data were collected along 5 parallel lines directed along the x-axis with a 0.01 m spatial offset, and at 0.10 m intervals along the y-axis. Each trace is 2 m long for Zone#2 and 1.7 m long for Zone#3.

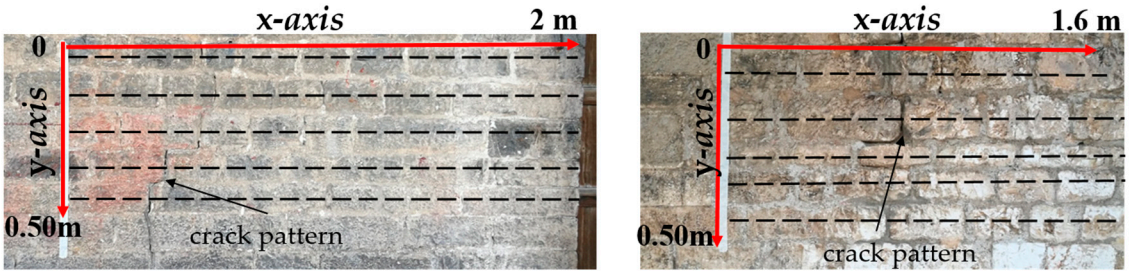

(**a**) (**b**)

Figure 6. (**a**) Measurement setup in Zone#2; (**b**) Measurement setup in Zone#3. The investigated areas were sampled about each 0.10 m along the y-axis (black dashed lines).

The visible crack patterns affecting these areas are less thick along the x-axis than the one affecting Zone#1. More precisely, the visible size is about 0.01 m, and thus less than the spatial resolution limit achievable with the adopted GPR system. Accordingly, it is expected that the tomographic images do not provide information concerning crack status, in terms of depth and width, but only allow an improvement of the available knowledge about the internal wall arrangement.

The tomographic images, referred to the (x,z) plane, for each acquisition line at Zone#2 and Zone#3, are shown into the left and right panels of Figure 7, respectively. These images have been obtained by using the TG procedure in the pre-processing step.

The left panel of Figure 7 shows the presence of two interfaces, occurring at each acquisition line of the Zone#2. Specifically, the first interface is located at z = 0.15 m, while the second one does not occur at a constant depth, and goes from a minimum depth of z = 0.40 m to a maximum depth of z = 0.80 m.

The right panel of Figure 7 shows that, similar to Zone#2, Zone#3 also shows a constant interface occurring at z = 0.15 m in all the tomographic images (see Figure 7a–e). Moreover, a second interface appears at a depth ranging from z = 0.40 m to z = 0.60 m in Figure 7a,b, with an anomaly, highlighted by a dashed white circle, always appearing around the point (x = 0.60 m, z = 0.80 m).

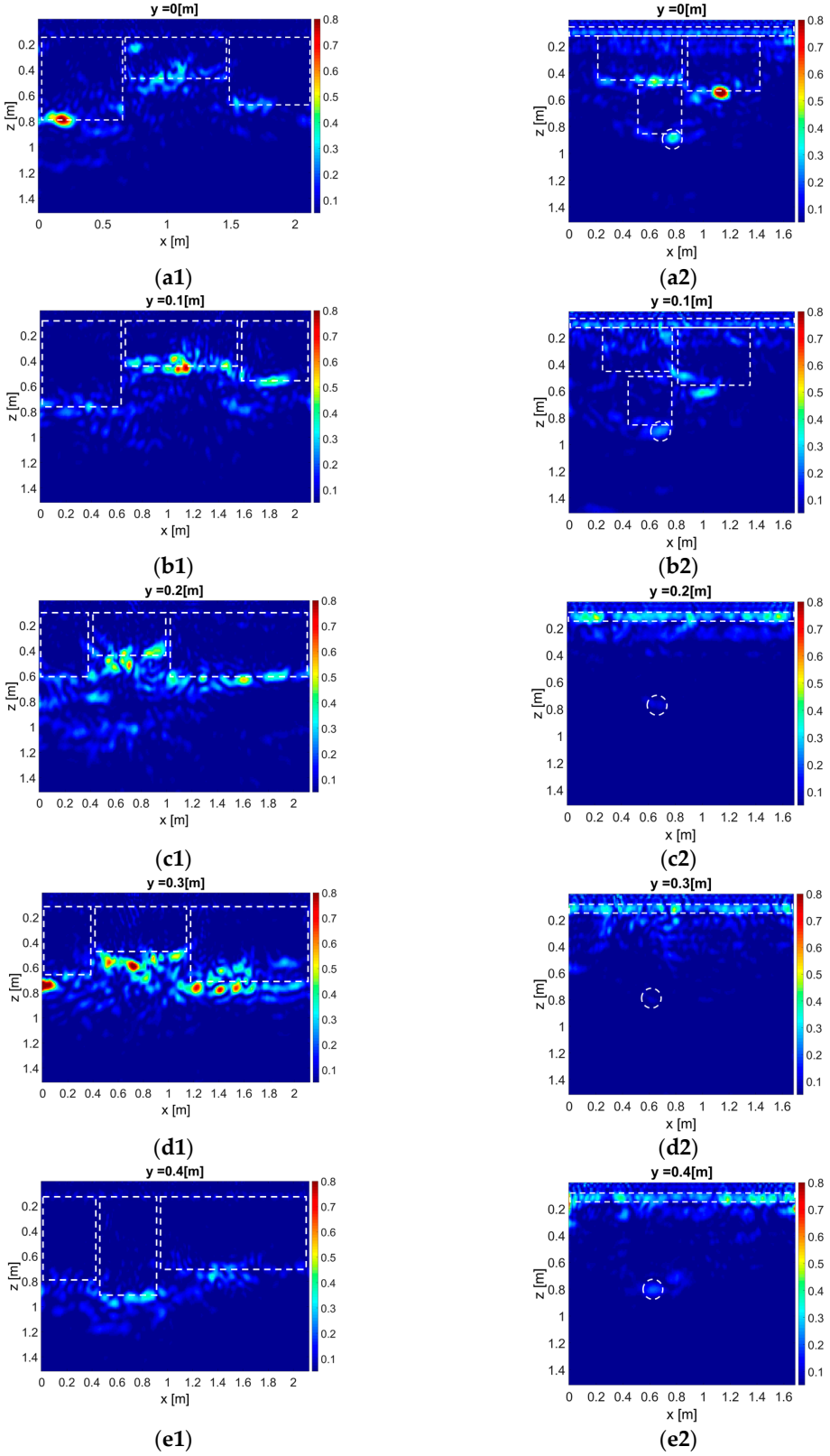

Figure 7. Tomographic images of the internal structures of the walls in Zone#2 (**left panels—a1–e1**) and in Zone#3 (**right panels—a2–e2**). The tomographic images show the normalized intensity of the obtained contrast.

4. Discussion

The results of the microwave tomography-enhanced GPR surveys performed are valuable in terms of improving the available knowledge regarding the structural status of the Loggia, and providing hints about its construction modalities. Indeed, as described in the previous section, and with reference to the areas investigated, these surveys allow:

(i) the imaging of inner wall texture, which is useful for inferring information about the construction modalities of the investigated regions;
(ii) the detection, localization and characterization of surface and subsurface anomalies—for example, cracks and fractures—provided that their size is comparable to or higher than the achievable spatial resolution.

Both of these kinds of information represent useful data for properly assessing the maintenance and degradation status of the Loggia.

Specifically, as is possible to infer by observing Figure 5 and the multimedia file (Figure S1), both concerning the Zone#1, the crack affecting this zone reaches a depth of about 0.10 m, while the first, second and third cavities reach depths about 0.13 m, 0.11 m, and 0.07 m, respectively. These results, jointly with direct observation, give hints about the structure of the brick wall by suggesting that the wall is made of layers stuck together with mortar, and allow an estimation of the thickness of the bricks, which is about 0.13 m. Therefore, the cracking phenomenon affects only the first layer of bricks.

On the other hand, the tomographic images, for depths greater than z = 0.20 m, allowed us to retrieve information concerning the global thickness of the brick wall and the internal arrangement of the stone walls. Specifically, based on the depth slices from z = 0.45 m to z = 0.64 m, three stone blocks, which are 0.70 m long and whose arrangement is similar to that of the surface stones (see Figure 5e), appear. Therefore, both the brick and stone parts of the wall appear to be layered structures, which are combined with each other by means of a joint structure like a zip. Furthermore, by taking into account the depth slices from z = 0.65 m to z = 0.71 m, it is possible to recognize the interface between the stone and the brick parts of wall, by observing that the stone part appears as a homogeneous medium, while the brick part is quite non-homogeneous (see Figure 5f). Finally, the depth slices at z greater than 0.72 m show the other side of the brick wall, i.e., the brick wall-air interface.

The tomographic images referring to Zone#2 and Zone#3 show the presence of a constant interface at depth z = 0.15 m. This suggest that the perimeter wall is made by an external layer of stones with a width of about 0.15 m, like the stone portion of the wall of the Loggia cross hall (Zone#1). On the other hand, the inner interface appearing at a non-constant depth suggests the presence of a second layer of stones, which have a width ranging from about 0.40 m to 0.70 m. It is worth noting that the fact that the inner interface does not appear in all of the images, and is not characterized by the same intensity, could be related to varying deterioration status of the mortar. Specifically, one could infer that where the inner interface is clearly visible, the mortar is largely missing, and is substituted by air [29].

Finally, the anomaly highlighted by the white circle in the tomographic images concerning Zone#3 could be associated with voids or metallic objects located behind the wall, where there is a spiral staircase leading to the upper floor, see Figure 3b.

5. Conclusions

This paper has presented the results of microwave tomography-enhanced GPR surveys carried out at Consoli Palace of Gubbio in July 2017. These results allowed an improved knowledge of its construction modalities, as well as of deterioration phenomena related to material aging and structural issues, of course with reference to the investigated wall parts. Specifically, as detailed in the discussion section, microwave tomography-enhanced GPR surveys allowed us to estimate the deep of crack and voids in Zone#1, and the depth of the inner stone layers.

It is worth noting that, in future, this information will be correlated to data provided by an extensometer. Specifically, based on the results prevented, further GPR measurements have been planned at Zone#1, and all of the obtained results will be related to the data provided by the extensometer located below this Zone (see Figure 4, wherein the extensometer is the copper bar). This future work aims, on one hand, to assess the usefulness of a diagnostic protocol exploiting different technologies and, on the other hand, to monitor the structural hazards affecting the cross hall leading to the Loggia over a temporal range of at least one year.

In this paper, data filtering procedures were selected by taking into account the peculiarity of the investigated scenarios, and a microwave tomography approach was selected as an advanced imaging procedure. In this context, future work will address the implementation of other advanced data-processing strategies, such as 2D and 3D migration approaches [17,18], and the full 3D microwave tomography approach proposed in [16]. In particular, we aim to utilize the data set referring to Zone#1 as a benchmark for comparing the imaging performances of the different approaches.

Supplementary Materials: The following are available online at www.mdpi.com/2072-4292/10/1/45/s1, Figure S1: Tomographic images sequence Zone#1.gif.

Acknowledgments: This project has received funding from the European Union's Horizon 2020 research and innovation program under grant agreement No. 700395.

Author Contributions: Ilaria Catapano and Giovanni Ludeno carried out the following activities: (a) GPR surveys; (b) data processing; (c) results interpretation, writing the paper. Ilaria Catapano also contributed to planning and organizing the measurement campaign. Francesco Soldovieri reviewed the results obtained and their interpretation, and contributed in writing the paper. Francesco Tosti supported the planning and organization of the measurement campaign, and provided the description of the test site. Giuseppina Padeletti reviewed the paper.

Conflicts of Interest: The authors declare no conflict of interest.

References

1. Colette, A. *Case Studies on Climate Change and World Heritage*; UNESCO World Heritage Centre: Paris, France, 2007.
2. Daniels, D.J. Ground Penetrating Radar. In *IEE Radar, Sonar and Navigation Series 15*; IEE: London, UK, 2004.
3. Orlando, L.; Pezone, A.; Colucci, A. Modeling and testing of high frequency GPR data for evaluation of structural deformation. *NDT E Int.* **2010**, *43*, 216–230. [CrossRef]
4. Chang, C.W.; Lin, C.H.; Lien, H.S. Measurement radius of reinforcing steel bar in concrete using digital image GPR. *Constr. Build. Mater.* **2009**, *23*, 1057–1063. [CrossRef]
5. Beben, D.; Mordak, A.; Anigacz, W. Identification of viaduct beam parameters using the Ground Penetrating Radar (GPR) technique. *NDT E Int.* **2012**, *49*, 18–26. [CrossRef]
6. Diamanti, N.; Giannopoulos, A.; Forde, M.C. Numerical modelling and experimental verification of GPR to investigate ring separation in brick masonry arch bridges. *NDT E Int.* **2008**, *41*, 354–363. [CrossRef]
7. Santos-Assunçao, S.; Perez-Gracia, V.; Caselles, O.; Clapes, J.; Salinas, V. Assessment of Complex Masonry Structures with GPR Compared to Other Non-Destructive Testing Studies. *Remote Sens.* **2014**, *6*, 82208–82237. [CrossRef]
8. Solla, M.; Lorenzo, H.; Riveiro, B.; Rial, F.I. Non-destructive methodologies in the assessment of the masonry arch bridge of Traba, Spain. *Eng. Fail. Anal.* **2011**, *18*, 828–835. [CrossRef]
9. Binda, L.; Zanzi, L.; Lualdi, M.; Condoleo, P. The use of georadar to assess damage to a masonry Bell Tower in Cremona, Italy. *NDT E Int.* **2005**, *38*, 171–199. [CrossRef]
10. Perez-Gracia, V.; Garcıa Garcıa, F.; Rodriguez Abad, I. GPR evaluation of the damage found in the reinforced concrete base of a block of flats: A case study. *NDT E Int.* **2008**, *41*, 341–353. [CrossRef]
11. Shaaban, F.A.; Abbas, A.M.; Atya, M.A.; Hafez, M.A. Ground-penetrating radar exploration for ancient monuments at the Valley of Mummies—Kilo 6, Bahariya Oasis, Egypt. *J. Appl. Geophys.* **2009**, *68*, 194–202. [CrossRef]
12. González-Drigo, R.; Pérez-Gracia, V.; Di Capua, D. GPR survey applied to modernista buildings in Barcelona: The cultural heritage of the College of Industrial Engineering. *J. Cult. Heritage* **2008**, *9*, 196–202. [CrossRef]
13. Soldovieri, F.; Hugenschmidt, J.; Persico, R.; Leone, G. A linear inverse scattering algorithm for realistic GPR applications. *Near Surf. Geophys.* **2007**, *5*, 29–42. [CrossRef]

14. Catapano, I.; di Napoli, R.; Soldovieri, F.; Bavusi, M.; Loperte, A.; Dumoulin, J. Structural monitoring via microwave tomography-enhanced GPR: The Montagnole test site. *J. Geophys. Eng.* **2012**, *9*, S100–S107. [CrossRef]
15. Kadioglu, S.; Kadioglu, Y.K.; Catapano, I.; Soldovieri, F. Ground penetrating radar and microwave tomography for the safety management of a cultural heritage site: Miletos Ilyas Bey Mosque (Turkey). *J. Geophys. Eng.* **2013**, *10*, 064007. [CrossRef]
16. Catapano, I.; Affinito, A.; Gennarelli, G.; di Maio, F.; Loperte, A.; Soldovieri, F. Full three-dimensional imaging via ground penetrating radar: Assessment in controlled conditions and on field for archaeological prospecting. *Appl. Phys. A* **2013**, *115*, 1415–1422. [CrossRef]
17. Gazdag, J. Wave equation migration with the phase shift method. *Geophysics* **1978**, *43*, 1342–1351. [CrossRef]
18. Lopez-Sanchez, J.M.; Fortuny-Guasch, J. 3-D radar imaging using range migration techniques. *IEEE Trans. Antennas Propag.* **2000**, *48*, 728–737. [CrossRef]
19. Marklein, R.; Mayer, K.; Hannemann, R.; Krylow, T.; Balasubramanian, K.; Langenberg, K.J.; Schmitz, V. Linear and nonlinear algorithms applied in nondestructive evaluation. *Inveres Probl.* **2002**, *18*, 1733–1757. [CrossRef]
20. Soldovieri, F.; Crocco, L. *Electromagnetic Tomography*; Vertiy Subsurface Sensing; Ahmet, S., Turk Koksal, A., Hocaoglu Alexey, A., Eds.; Wiley: Hoboken, NJ, USA, 2011.
21. González-Huici, M.A.; Catapano, I.; Soldovieri, F. A comparative study of GPR reconstruction approaches for landmine detection. *IEEE J. Sel. Top. Appl. Earth Obs. Remote Sens.* **2014**, *7*, 4869–4878. [CrossRef]
22. IDS Georadar Website. Available online: https://idsgeoradar.com/products (accessed on 1 August 2017).
23. Catapano, I.; Affinito, A.; Soldovieri, F. An improved interface to process GPR data by means of microwave tomography. In Proceedings of the EGU General Assembly, Vienna, Austria, 12–17 April 2015; id.13061.
24. Bertero, M. Linear inverse and ill-posed problems. *Adv. Electron. Electron. Phys.* **1989**, *45*, 1–120.
25. Persico, R.; Soldovieri, F. Effects of uncertainty on background permittivity in one-dimensional linear inverse scattering. *J. Opt. Soc. Am. A* **2004**, *21*, 2334–2343. [CrossRef]
26. Moore, J.C.; Pälli, A.; Ludwing, F.; Blatter, H.; Jania, J.; Gadek, B.; Glowacki, P.; Mochnacki, D.; Isaksson, E. High-resolution hydrothermal structure of Hansbreen, Spitsbergen, mapped by ground-penetrating radar. *J. Glaciol.* **1999**, *45*, 524–532. [CrossRef]
27. Pettinelli, E.; Vannaroni, G.; Cereti, A.; Paolucci, F.; della Monica, G.; Storini, M.; Bella, F. Frequency and time domain permittivity measurements on solid CO_2 and solid CO_2–soil mixtures as Martian soil simulants. *J. Geophys. Res.* **2003**, *108*, 8029. [CrossRef]
28. Olatinsu, O.B.; Olorode, D.O.; Oyedele, K.F. Radio frequency dielectric properties of limestone and sandstone from Ewekoro, Eastern Dahomey Basin. *Adv. Appl. Sci. Res.* **2013**, *4*, 150–158.
29. Bavusi, M.; Soldovieri, F.; Piscitelli, S.; Loperte, A.; Vallianatos, F.; Soupios, P. Ground-penetrating radar and microwave tomography to evaluate the crack and joint geometry in historical buildings: Some examples from Chania, Crete, Greece. *Near Surf. Geophys.* **2010**, *8*, 3773–3787. [CrossRef]